Small Angle Scattering and Large Scale Structures

H. Frielinghaus

This document has been published in

Manuel Angst, Thomas Brückel, Dieter Richter, Reiner Zorn (Eds.):
Scattering Methods for Condensed Matter Research: Towards Novel Applications at Future Sources
Lecture Notes of the 43rd IFF Spring School 2012
Schriften des Forschungszentrums Jülich / Reihe Schlüsseltechnologien / Key Technologies, Vol. 33
JCNS, PGI, ICS, IAS
Forschungszentrum Jülich GmbH, JCNS, PGI, ICS, IAS, 2012
ISBN: 978-3-89336-759-7

D 1 Small Angle Scattering and Large Scale Structures[1]

H. Frielinghaus
Jülich Centre for Neutron Science
Forschungszentrum Jülich GmbH

Contents

---

[1] Lecture Notes of the 43^{rd} IFF Spring School "Scattering Methods for Condensed Matter Research: Towards Novel Applications at Future Sources" (Forschungszentrum Jülich, 2012). All rights reserved.

1 Introduction

Scattering methods have to be seen in context to direct imaging methods (such as microscopy). The wavelength of the probe gives a good guess for the accessible structural sizes to be resolved – in either case it is connected to a lower boundary. Especially for the probes neutrons and x-rays, small angle scattering opens a window on the nanometer length scales. These length scales are highly interesting as mesoscales where the atomistic properties are overcome and many body effects come into play. A lot of macroscopic properties can only be explained on the basis of mesoscopic length scale effects. Theoretical understanding, modeling and small angle scattering are tightly linked.

Historically, lens systems for neutrons and x-rays were not accessible and, thus, the only way to the nanometer length scales were scattering experiments [1, 2]. While direct images are intuitively understandable, scattering experiments have to be understood on the basis of the Fourier transformation. While for well ordered crystals the understanding remains a simple task (note Bragg's law) for many mesoscopic effects the scattering patterns demand for more complicated modeling. Nonetheless, scattering models have been and are developed for the focus of the actual research, and apart from that, plausible arguments are found for many practical applications such that the experienced small angle scatterer sees a lot of details at first hand before tedious modeling is applied.

Nowadays, electron microscopy has become a strong tool to probe the nano-world. It has to be mentioned, that often surfaces (of fractures) are characterized. Single images are only excerpts of the whole story – sometimes one even has to worry whether the conditions of preparation represent the desired condition. Apart from that, average magnitudes – such as particle sizes – have to be counted from many measurements. The scattering experiments are in most of the cases in situ experiments. The sample can be kept at a certain temperature, pressure, magnetic and electric field – even shear and flow fields can be applied. In most of the cases, rather large volumes are irradiated, and so an average impression is obtained from macroscopic volumes. So, for instance, the obtained particle sizes base on good statistics.

A good example for small angle scattering are polymer systems. A polymer is a linear molecule of identical monomeric units – so polystyrene is made of the styrene monomer. The monomer properties are to be understood (more or less) as atomistic effects, and mainly the connectivity of the monomers is responsible for the mesoscopic understanding which finally ends in a coil-shaped linear molecule. The small angle scattering experiment especially focuses on the connectivity and is able to resolve the overall dimension of the single molecule. If chemically different polymers form a compound material, often nanometer domains form – so the polymers tend to phase separation. These domains can be tailored by the thermal history, but also by chemical additives (such as diblock copolymers) which support the miscibility by keeping the domains small at a desired size. Still, these length scales are of several tens to hundreds of nanometers and are ideally observed by small angle scattering. The mixing of polymers leads to mixed macroscopic properties – so often mechanic properties are tailored from originally individual favorable properties such as softness, rubber elasticity, and mechanical strength. A microscopic understanding of these effects is invaluable.

Complex fluids consist of at least two components. In the case of microemulsions oil and water are mixed macroscopically homogenously – but microscopically still domains of oil and water form on the nano-scale. The added surfactant makes the microemulsion thermodynamically stable and controls the domain size. Additives like amphiphilic polymers tailor the overall properties of the amphiphile. Often, the surfactant film becomes stiffer, and larger domains can

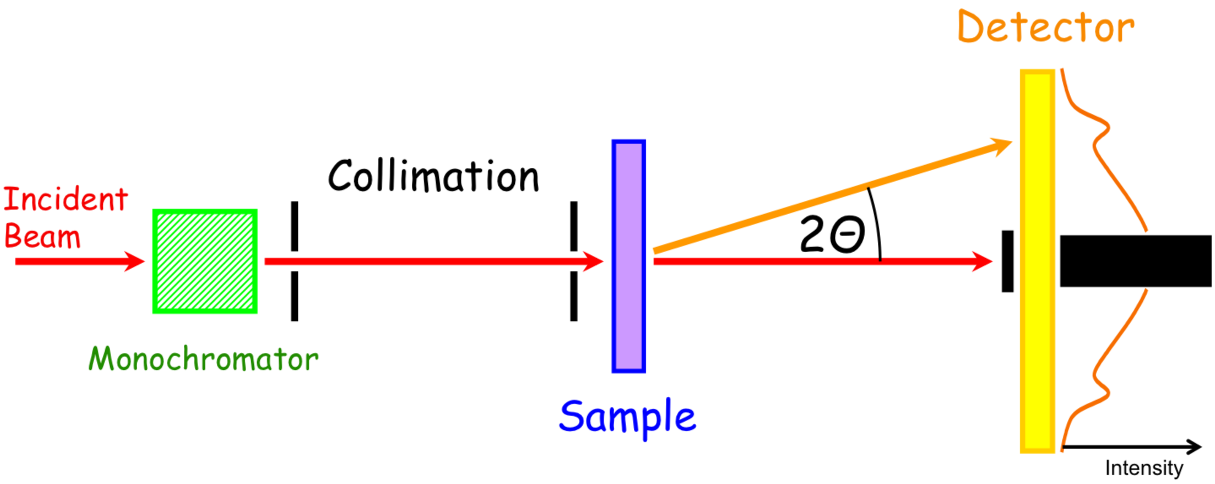

Fig. 1: *Scheme of a small angle neutron scattering instrument. The neutrons pass from the left to the right. The incident beam is monochromated and collimated before it hits the sample. Non-scattered neutrons are absorbed by the beam stop in the center of the detector. The scattered neutron intensity is detected as a function of the scattering angle* 2θ.

form. All these effects were monitored by small angle neutron scattering experiments.

2 Small Angle Neutron Scattering

The first small angle neutron scattering instruments have been developed for continuous sources realized by research reactors. The neutrons are moderated by the cold source to ca. 20-30K. Typical wavelengths are found between 4 and 6Å, and reasonable intensities are obtained up to 20Å. A typical scheme of a small angle neutron scattering (SANS) instrument is depicted in Figure 1. The cold neutrons can easily be guided by mirror coated cavities to the instrument. The first important element is the neutron velocity selector (Fig. 2). It consists of tilted lamellae on a rotating cylinder which selects the desired neutron velocity mechanically. The wavelength uncertainty results from the gap width and length between the lamellae and typically takes values of ±5 to ±10%. Then the collimation is formed by an entrance aperture and the sample aperture with a certain distance L_C on which the neutrons propagate freely. For varying the collimation distance, the neutrons are guided with movable 1m neutron guides to the desired distance relatively to the fixed sample position. Very often, the maximum length is 20 meters, but other examples exist with 6 over 10 to 40m. The sample is placed directly behind the sample diaphragm (see sample position on Fig. 3). Most of the neutrons (between 50 and 90%) pass the sample unscattered. In front of the detector a beam stop absorbs these high intensities because the highly sensitive detector does not serve this high dynamic range. The scattered neutrons are detected on a position sensitive area detector. In this way, the scattering intensity is monitored as a function of the scattering angle 2θ. Typical sizes of the beam stop are $4\times4\mathrm{cm}^2$, and for the sensitive area between 60×60 to $100\times100\mathrm{cm}^2$. For varying the covered angle, the detector is placed at different distances L_D (symmetrically to the collimation distance L_C) inside a large vacuum tube.

Fig. 2: *The neutron velocity selector of the small angle scattering instrument KWS-3 at the research reactor Garching FRM-2. This selector was especially manufactured for larger wavelengths (above 7Å).*

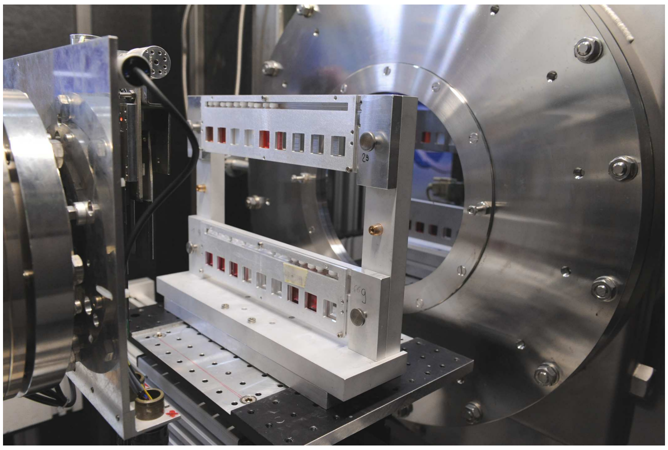

Fig. 3: *View on the sample position of the small angle scattering instrument KWS-1 at the research reactor Garching FRM-2. The neutrons come from the left through the collimation and sample aperture (latter indicated). A sample changer allows for running 27 samples (partially colored solutions) in one batch file. The silicon window to the detector tube is seen behind.*

2.1 The scattering vector Q

In this section, the scattering vector $\mathbf{Q}$ is described with its experimental uncertainty. The scattering process is schematically shown in Fig. 4, in real space and momentum space. In real space the beam hits the sample with a distribution of velocities (magnitude and direction). The neutron speed is connected to the wavelength, whose distribution is depending on the velocity selector. The directional distribution is defined by the collimation. After the scattering process, the direction of the neutron is changed, but the principal inaccuracy remains the same. The scattering angle 2θ is the azimuth angle. The remaining polar angle is not discussed further here. For samples with no preferred direction the scattering is isotropic and, thus, does not depend on the polar angle. In reciprocal space the neutrons are defined by the wave vector $\mathbf{k}$. The main direction of the incident beam is defined as the z-direction, and the modulus is determined by the wavelength, so $|\mathbf{k}_i| = 2\pi/\lambda$. Again, $\mathbf{k}$ is distributed due to the selector and the collimation inaccuracies. The wave vector of the (quasi) elastic scattering process has the same modulus, but differs in direction, namely by the angle 2θ. The difference between both wave vectors is given by the following value:

$$Q = \frac{4\pi}{\lambda} \sin\theta \tag{1}$$

For isotropic scattering samples, the measured intensity depends only on the absolute value of the scattering vector $Q = |\mathbf{Q}|$. For small angles, the common approximation of small angle (neutron) scattering is valid:

$$Q = \frac{2\pi}{\lambda} \cdot 2\theta \tag{2}$$

The typical Q-range of a small angle scattering instrument thus follows from the geometry. The detector distances L_D vary in the range from 1m to 20m. The area detector is active between

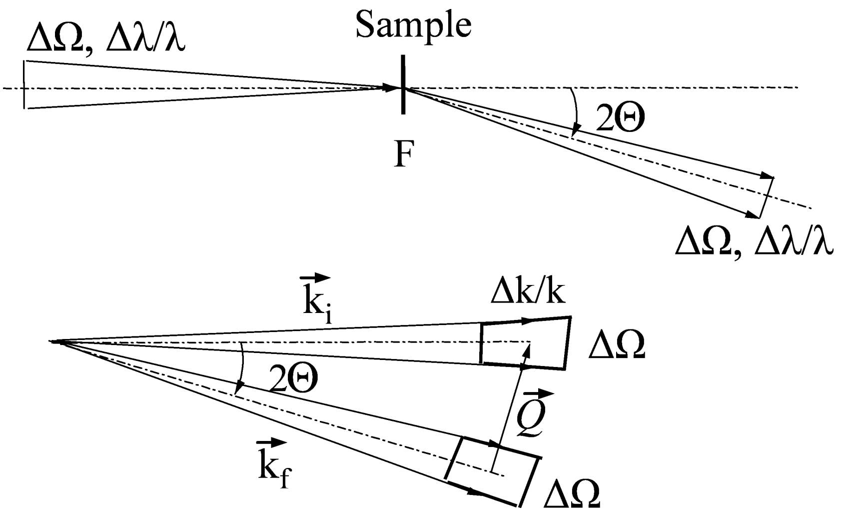

Fig. 4: Top: *the neutron speed and its distribution in real space, before and after the scattering process.* Bottom: *The same image expressed by wave vectors (reciprocal space). The scattering vector is the difference between the outgoing and incoming wave vector.*

$\varnothing_D = 2$cm and 35cm from the center. The angle 2θ is approximated by the ratio $\varnothing_D/L_D$ and the wavelength λ is 7Å. For the two SANS instruments KWS-1 and KWS-2 at the research reactor Garching FRM-2, a typical Q-range from $1{\times}10^{-3}$ to 0.3Å^{-1} is obtained.
The Q-vector describes which length scales ℓ are observed, following the rule $\ell = 2\pi/Q$. If a Bragg peak is observed, the lattice parameters can be taken directly from the position of the peak. If the scattering shows a sudden change at a certain Q-value, we obtain the length scale of the structural differences. There are characteristic scattering behaviors that can be described by so called scattering laws that are simple power laws Q^α with different exponents α.

2.2 The Fourier transformation in the Born approximation

This section deals with the physical explanation for the appearance of the Fourier transformation in the Born approximation. In simple words, in a scattering experiment one observes the intensity as the quadrature of the Fourier amplitudes of the sample structure. This is considerably different from microscopy where a direct image of the sample structure is obtained. So the central question is: Where does the Fourier transformation come from?
The classical SANS instruments are also called pin-hole instruments. Historically, pin-hole cameras were discovered as the first cameras. They allowed to picture real sceneries on blank screens – maybe at different size, but the image resembled the original picture. The components of this imaging process are depicted in Fig. 5. Let's assume the following takes place with only one wavelength of light. The original image is then a monochromatic picture of the three numbers 1, 2 and 3. The corresponding rays meet in the pin-hole, and divide afterwards. On the screen, the picture is obtained as a real-space image, just appearing upside down. From experience we know, that the screen may be placed at different distances resulting in different sizes of the image. The restriction of the three beams through the pin-hole holds for the right space behind the pin-hole. In front of the pin-hole the light propagates also in other directions – it is just absorbed by the wall with the pin-hole.
So far, we would think that nothing special has happened during this process of reproduction. But what did happen to the light in the tiny pin-hole? We should assume that the size of the pin-

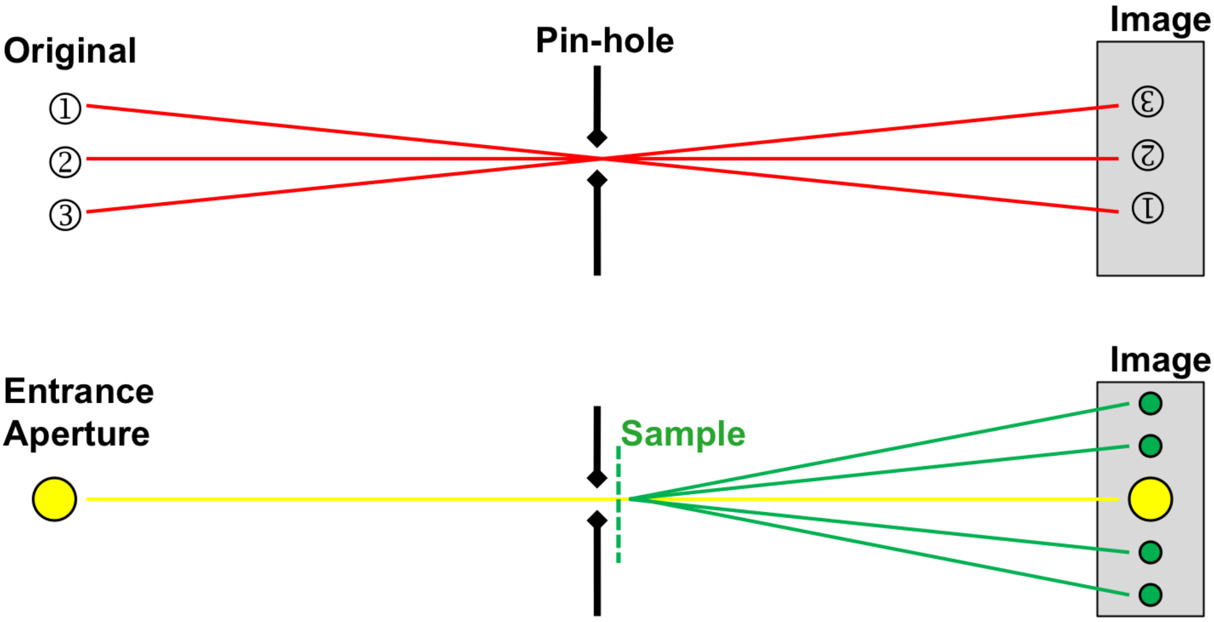

Fig. 5: *The principle of a pin-hole camera transferred to the pin-hole SANS instrument.* Top: *The pin-hole camera depicts the original image (here consisting of three numbers). For simplicity, the three points are represented by three rays which meet in the pin-hole, and divide afterwards. On the screen, a real space image is obtained (upside down).* Bottom: *The pin-hole SANS instrument consists of an entrance aperture which is depicted on the detector through the pin-hole (same principle as above). The sample leads to scattering. The scattered beams are shown in green.*

hole is considerably larger than the wavelength. Here, the different rays of the original image interfere and inside the pin-hole a wave field is formed. The momentum along the optical z-axis indicates the propagation direction and is not very interesting (because is nearly constant for all considered rays). The momenta in the x-y-plane are much smaller and indicate a direction. They originate from the original picture and remain constant during the whole process. Before and after the pin-hole the rays are separated and the directions are connected to a real-space image. In the pin-hole itself the waves interfere and the wave field looks more complicated. The information about the original scenery is conserved through all the stages. That means that also the wave field inside the pin-hole is directly connected to the original picture.

From quantum mechanics (and optics) we know that the vector of momentum is connected to a wave vector. This relation describes how the waves inside the pin-hole are connected to a spectrum of momenta. In classical quantum mechanics (for neutrons) a simple Fourier transformation describes how a wave field in real space (pin-hole state) is connected with a wave field in momentum space (separated beams). In principle, the interpretation is reversible. For electromagnetic fields (for x-rays) the concept has to be transferred to particles without mass. Overall, this experiment describes how the different states appear and how they are related. The free propagation of a wave field inside a small volume (pin-hole) leads to a separation of different rays accordingly to their momentum.

Now we exchange the original image by a single source (see yellow spot in lower part of Fig. 5). This source is still depicted on the image plate (or detector). If we insert a sample at the position of the pin-hole the wave field starts to interact with the sample. In a simplified way we can say that a small fraction of the wave field takes the real space structure of the sample

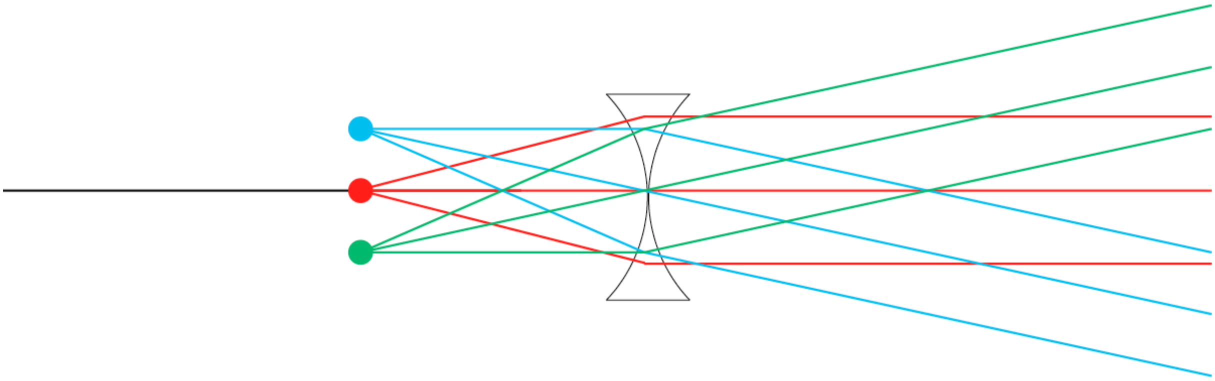

Fig. 6: *How a Fourier transformation is obtained with refractive lenses. The real space structure in the focus of the lens is transferred to differently directed beams. The focusing lens is concave since for neutrons the refractive index is smaller than 1.*

while the major fraction passes the sample without interaction. This small fraction of the wave field resulting from the interaction propagates freely towards the image plate and generates a scattering pattern. As we have learned, the momenta present in the small fraction of the wave field give rise to the separation of single rays. So the real space image of the sample leads to a Fourier transformed image on the detector. This is the explanation how the Fourier transformation appears in a scattering experiment – so this is a simplified motivation for the Born approximation. A similar result was found by Fraunhofer for the diffraction of light at small apertures. Here, the aperture forms the wave field (at the pin-hole) and the far field is connected to the Fourier transformation of the aperture shape.

Later we will see that the size of wave field packages at the pin-hole is given by the coherence volume. The scattering appears independently from such small sub-volumes and is a simple superposition.

2.3 Remarks on focusing SAS instruments

Small angle scattering instruments with focusing optics allow for larger samples. If the entrance aperture remains at the old size the resolution of the experiment is kept, but the intensity is increased tremendously. If the entrance aperture is closed by considerable factors the resolution is increased strongly, and much lower scattering vectors (larger structures) are resolved. Usually, the entrance aperture must have a minimum size for a minimal intensity. For a symmetric set-up (collimation and detector distance equal, i.e. $L_C = L_D$) the focusing optic is in the middle at the sample position. The focus f is half the collimation distance, i.e. $f = \frac{1}{2}L_C = \frac{1}{2}L_D$. Now the places where exact Fourier transforms are obtained (from the entrance aperture and from the sample structure) do not agree anymore. The sample is still considered as a small volume and from there the waves propagate freely to the detector, and the already known relation between sample structure and scattering image holds.

For focusing elements, the places of Fourier transformations differ (see Fig. 6). The original structure is placed in the focus, and the resulting distinctive rays are obtained at the other side of the lens in the far field. So for focusing SAS instruments, the places of appearing Fourier transformations for the entrance aperture and the sample structure differ.

The historical development of cameras can be seen in parallel. The first cameras were pin-hole cameras, but when lenses could be manufactured lens cameras replaced the old ones. The direct advantage was the better light yield being proportional to the lens size. Another effect appeared: The new camera had a depth of focus – so only certain objects were depicted sharply, which was welcomed in the art of photography. The focusing SAS instrument depicts only the entrance aperture, and the focusing is not a difficult task. The higher intensity or the better resolution are the welcomed properties of the focusing SAS instrument.

2.4 The resolution of a SANS instrument

The simple derivatives of equation 2 support a very simple view on the resolution of a small angle neutron scattering experiment. We obtain:

$$\left(\frac{\Delta Q}{Q}\right)^2 = \left(\frac{\Delta\lambda}{\lambda}\right)^2 + \left(\frac{2\Delta\theta}{2\theta}\right)^2 \tag{3}$$

The uncertainty about the Q-vector is a sum about the uncertainty of the wavelength and the angular distribution. Both uncertainties result from the beam preparation, namely from the monochromatization and the collimation. The neutron velocity selector selects a wavelength band of either ±5% or ±10%. The collimation consists of an entrance aperture with a diameter d_C and a sample aperture of a diameter d_S. The distance between them is L_C.

One property of eq. 3 is the changing importance of the two contributions at small and large Q. At small Q the wavelength spread is nearly negligible and the small terms Q and θ dominate the resolution. This also means that the width of the primary beam is exactly the width of the resolution function. More exactly, the primary beam profile describes the resolution function at small Q. Usually, the experimentalist is able to change the resolution at small Q. At large Q the resolution function is dominated by the wavelength uncertainty. So the experimentalist wants to reduce it – if possible – for certain applications. This contribution is also an important issue for time-of-flight SANS instruments at spallation sources. The wavelength uncertainty is determined by the pulse length of the source and cannot be reduced without intensity loss.

A more practical view on the resolution function includes the geometrical contributions explicitly [3]. One obtains:

$$\left(\frac{\sigma_Q}{Q}\right)^2 = \frac{1}{8\ln 2}\left(\left(\frac{\Delta\lambda}{\lambda}\right)^2 + \left(\frac{1}{2\theta}\right)^2 \cdot \left[\left(\frac{d_C}{L_C}\right)^2 + d_S^2\left(\frac{1}{L_C}+\frac{1}{L_D}\right)^2 + \left(\frac{d_\mathrm{D}}{L_D}\right)^2\right]\right) \tag{4}$$

Now the wavelength spread is described by $\Delta\lambda$ being the full width at the half maximum. The geometrical terms have contributions from the aperture sizes d_C and d_S and the spatial detector resolution d_D. The collimation length L_C and detector distance L_D are usually identical such that all geometric resolution contributions are evenly large ($d_C = 2d_S$ then). This ideal setup maximizes the intensity with respect to a desired resolution.

The resolution function profile is another topic of the correction calculations. A simple approach assumes Gaussian profiles for all contributions, and finally the overall relations read:

$$\left.\frac{d\Sigma(\bar{Q})}{d\Omega}\right|_{\mathrm{meas}} = \int_0^\infty dQ\; R(Q-\bar{Q}) \cdot \left.\frac{d\Sigma(Q)}{d\Omega}\right|_{\mathrm{theo}} \tag{5}$$

$$R(Q-\bar{Q}) = \frac{1}{\sqrt{2\pi}\sigma_Q}\exp\left(-\frac{1}{2}\frac{(Q-\bar{Q})^2}{\sigma_Q^2}\right) \tag{6}$$

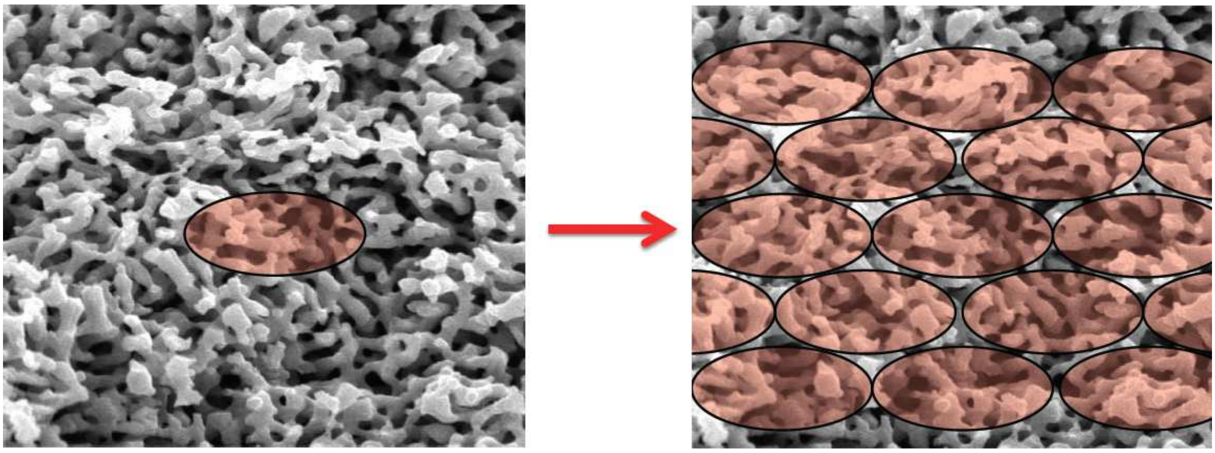

Fig. 7: *The coherence volume is usually much smaller than the sample volume (left). So the overall scattering appears as an incoherent superposition of the scattering from many coherence volumes (right).*

The theoretical macroscopic cross section is often described by a model function which is fitted to the experimental data. In this case the computer program only does a convolution of the model function with the resolution function $R(\Delta Q)$. Alternatively, there are methods to deconvolute the experimental data without modeling the scattering at first hand.

The here described resolution function is given as a Gaussian. This is true for relatively narrow distributions. The reason for using a Gaussian function although the original distributions of λ and θ are often triangular is: The central limit theorem can be applied to this problem because we have seen from eq. 4 that there are four contributions to the resolution function, and the radial averaging itself also smears the exact resolution function further out. Thus, the initial more detailed properties of the individual distributions do not matter anymore. Equations 5 and 6 are a good approximation for many practical cases.

We now want to describe the connection between the resolution function and the coherence of the neutron beam at the sample position. From optics we know about the transverse coherence length:

$$\ell_{\text{coh,transv}} = \frac{\lambda L_C}{2d_C} \qquad \text{is similar to} \qquad \Delta Q_\theta^{-1} = \frac{\lambda L_C}{\pi d_C} \tag{7}$$

It can be compared well with the geometric resolution contribution that arises from the entrance aperture only. Small differences in the prefactors we can safely neglect. For the longitudinal coherence length we obtain:

$$\ell_{\text{coh,long}} = \frac{1}{4}\lambda\left(\frac{\Delta\lambda}{\lambda}\right)^{-1} \qquad \text{is similar to} \qquad \Delta k^{-1} = \frac{1}{2\pi}\lambda\left(\frac{\Delta\lambda}{\lambda}\right)^{-1} \tag{8}$$

This coherence length can be well compared to the wavevector uncertainty of the incoming beam. If we look back on Figure 4 we see that the coherence volume exactly describes the uncertainty of the incoming wave vector. The two contributions are perpendicular which supports the vectorial (independent) addition of the contributions in eq. 4 for instance. The coherence volume describes the size of the independent wave packages which allow for wave-like properties such as the scattering process. So the coherence volume describes the maximum size of structure that is observable by SANS. If larger structures need to be detected the resolution must be increased.

The understanding how the small coherence volume covers the whole sample volume is given in the following (see also Fig. 7). Usually the coherence volume is rather small and is many times smaller than the irradiated sample volume. So many independent coherence volumes cover the whole sample. Then, the overall scattering intensity occurs as an independent sum from the scattering intensities of all coherence volumes. This is called incoherent superposition.

2.5 The theory of the macroscopic cross section (the Born approximation)

We have seen that the SANS instrument aims at the macroscopic cross section which is a function of the scattering vector $\mathbf{Q}$. In many examples of isotropic samples and orientationally averaged samples (powder samples) the macroscopic cross section depends on the modulus $|\mathbf{Q}| \equiv Q$ only. This measured function has to be connected to important structural parameters of the sample. For this purpose model functions are developed. The shape of the model function in comparison with the measurement already allows to distinguish the validity of the model. After extracting a few parameters with this method, deeper theories – like thermodynamics – allow to get deeper insight about the behavior of the sample. Usually, other parameters – like concentration, temperature, electric and magnetic fields, ... – are varied experimentally to verify the underlying concepts at hand. The purpose of this and the following sections is to give some ideas about model functions.

We have obtained a clear picture of the Born approximation in section 2.2. More formally, the Born approximation arises from quantum mechanics, and several facts and assumptions came along: The scattering amplitudes of the outgoing waves are derived as perturbations of the incoming plane wave. The matrix elements of the interaction potential with these two wave fields as vectors describe the desired amplitudes. The interaction potential can be simplified for neutrons and the nuclei of the sample by the Fermi pseudo potential. This expresses the smallness of the nuclei ($\sim$1fm) in comparison to the neutron wavelength ($\sim$Å). For the macroscopic cross section we immediately obtain a sum over all nuclei:

$$\frac{d\Sigma}{d\Omega}(\mathbf{Q}) = \frac{1}{V}\left|\sum_j b_j \exp(\mathrm{i}\mathbf{Q}\cdot\mathbf{r}_j)\right|^2 \tag{9}$$

This expression is normalized to the sample volume V because the second factor usually is proportional to the sample size. This simply means: The more sample we put in the beam the more intensity we obtain. The second factor is the square of the amplitude because we measure intensities. While for electromagnetic fields at low frequencies one can distinguish amplitudes and phases (without relying on the intensity) the neutrons are quantum mechanical particles where experimentally such details are hardly accessible. For light (and neutrons) for instance holographic methods still remain. The single amplitude is a sum over each nucleus j with its typical scattering length b_j and a phase described by the exponential. The square of the scattering length b_j^2 describes a probability of a scattering event taking place for an isolated nucleus. The phase arises between different elementary scattering events of the nuclei for the large distances of the detector. In principle, the scattering length can be negative (for hydrogen for instance) which indicates an attractive interaction with a phase π. Complex scattering lengths indicate absorption. The quadrature of the amplitude can be reorganized:

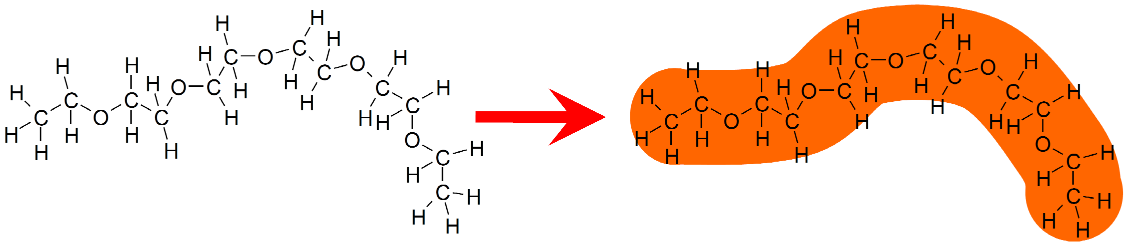

Fig. 8: *The concept of the scattering length density. On the left the atomic structure of a polyethylene oxide polymer (PEO) is depicted. For small angle scattering the wavelength is much larger than the atomic distance. So for SANS the polymer appears like a worm with a constant scattering length density inside.*

$$\frac{d\Sigma}{d\Omega}(\mathbf{Q}) = \frac{1}{V}\sum_{j,k} b_j b_k \exp\left(\mathrm{i}\mathbf{Q}(\mathbf{r}_j - \mathbf{r}_k)\right) \tag{10}$$

Here we find then self-terms with identical indices j and k without any phase and cross terms with phases arising from distances between different nuclei. Here it becomes obvious that only relative positions of the nuclei matter which is a result of the quadrature. The overall phase of the sample does not matter because of the modulus in eq. 9. We will use this expression for the polymer scattering.

Apart from this detailed expression a simplified view is allowed for small angle scattering experiments. Firstly, we know that the wavelength is typically 7Å which is much larger than the atom-atom distance of ca. 1.5Å. Secondly, the SANS experiment aims at structures at the nano-scale. So the scattering vector aims at much larger distances compared to the atomistic distances (i.e. $2\pi Q^{-1} \gg 1$Å). This allows for exchanging sums by integrals as follows:

$$\sum_j b_j \cdots \quad \longrightarrow \quad \int_V d^3r\ \rho(\mathbf{r}) \cdots \tag{11}$$

Such methods are already known for classical mechanics, but reappear all over physics. The meaning is explained by the sketch of Figure 8. The polymer polyethylene oxide (PEO) contains many different nuclei of different species (hydrogen, carbon and oxide). However, the SANS method does not distinguish the exact places of the nuclei. The polymer appears rather like a homogenous worm. Inside, the worm has a constant scattering length density which reads:

$$\rho_{\mathrm{mol}} = \frac{1}{V_{\mathrm{mol}}} \sum_{j\in\{\mathrm{mol}\}} b_j \tag{12}$$

So, for each molecule we consider all nuclei and normalize by the overall molecule volume. Of course different materials have different scattering length densities ρ. The initial equation 9 reads then:

$$\begin{aligned} \frac{d\Sigma}{d\Omega}(\mathbf{Q}) &= \frac{1}{V}\left|\int_V d^3r\ \rho(\mathbf{r})\exp(\mathrm{i}\mathbf{Q}\mathbf{r})\right|^2 && (13) \\ &= \frac{1}{V}\left|\mathcal{F}\left[\rho(\mathbf{r})\right]\right|^2 \qquad = \frac{1}{V}\left|\rho(\mathbf{Q})\right|^2 && (14) \end{aligned}$$

The single amplitude is now interpreted as a Fourier transformation of the scattering length density $\rho(\mathbf{r})$ which we simply indicate by $\rho(\mathbf{Q})$. The amplitude is defined by:

$$\rho(\mathbf{Q}) = \int\limits_V d^3r \; \rho(\mathbf{r}) \exp(\mathrm{i}\mathbf{Q}\mathbf{r}) \tag{15}$$

Again, equation 13 loses the phase information due to the modulus.

2.6 Spherical colloidal particles

In this section we will derive the scattering of diluted spherical particles in a solvent. These particles are often called colloids, and can be of inorganic material while the solvent is either water or organic solvent. Later in the manuscript interactions will be taken into account.
One important property of Fourier transformations is that constant contributions will lead to sharp delta peaks at $Q = 0$. This contribution is not observable in the practical scattering experiment. The theoretically sharp delta peak might have a finite width which is connected to the overall sample size, but centimeter dimensions are much higher compared to the largest sizes observed by the scattering experiment ($\sim \mu$m). So formally we can elevate the scattering density level by any number $-\rho_{\text{ref}}$:

$$\rho(\mathbf{r}) \longrightarrow \rho(\mathbf{r}) - \rho_{\text{ref}} \qquad \text{leads to} \qquad \rho(\mathbf{Q}) \longrightarrow \rho(\mathbf{Q}) - 2\pi\rho_{\text{ref}}\delta(\mathbf{Q}) \tag{16}$$

The resulting delta peaks can simply be neglected. For a spherical particle we then arrive at the simple scattering length density profile:

$$\rho_{\text{single}}(\mathbf{r}) = \begin{cases} \Delta\rho & \text{for } |\mathbf{r}| \leq R \\ 0 & \text{for } |\mathbf{r}| > R \end{cases} \tag{17}$$

Inside the sphere the value is constant because we assume homogenous particles. The reference scattering length density is given by the solvent. This function will then be Fourier transformed accordingly:

$$\begin{aligned}
\rho_{\text{single}}(\mathbf{Q}) &= \int\limits_0^{2\pi} d\phi \int\limits_0^{\pi} d\vartheta \; \sin\vartheta \int\limits_0^{R} dr \; r^2 \; \Delta\rho \; \exp\big(\mathrm{i}|\mathbf{Q}| \cdot |\mathbf{r}| \cos(\vartheta)\big) && (18) \\
&= 2\pi \; \Delta\rho \int\limits_0^{R} dr \; r^2 \; \left[\frac{1}{\mathrm{i}Qr} \exp\big(\mathrm{i}QrX\big)\right]_{X=-1}^{X=+1} && (19) \\
&= 4\pi \; \Delta\rho \int\limits_0^{R} dr \; r^2 \; \frac{\sin(Qr)}{Qr} && (20) \\
&= \Delta\rho \; \frac{4\pi}{3} R^3 \left(3 \frac{\sin(QR) - QR\cos(QR)}{(QR)^3}\right) && (21)
\end{aligned}$$

In the first line 18 we introduce spherical coordinates with the vector $\mathbf{Q}$ determining the z-axis for the real space. The vector product $\mathbf{Q}\mathbf{r}$ then leads to the cosine term. In line 19 the

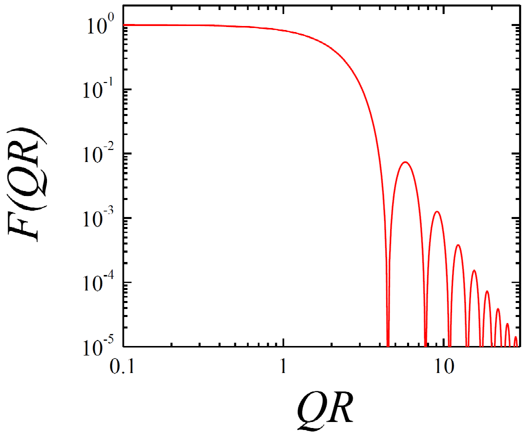

Fig. 9: *The form factor of a homogenous sphere in a double logarithmic plot.*

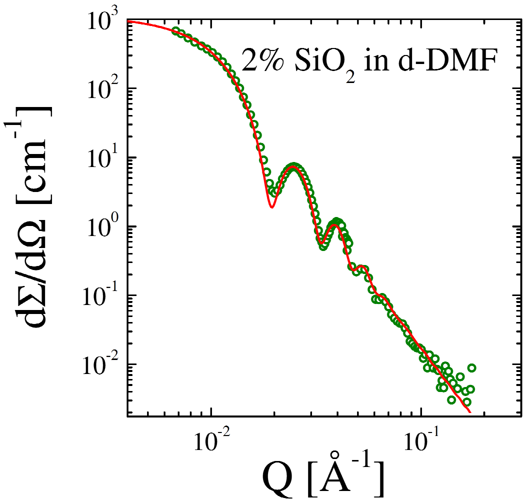

Fig. 10: *Experimental scattering curve of spherical SiO_2 colloids in the deuterated solvent DMF [4]. The resolution function (eq. 5) is included in the fit (red line).*

azimuthal integral is simply 2π, and the variable $X = \cos\vartheta$ is introduced. Finally, in line 20 the kernel integral for spherically symmetric scattering length density distributions is obtained. For homogenous spheres we obtain the final result of eq. 21. Putting this result together for the macroscopic cross section (eq. 14) we obtain:

$$\frac{d\Sigma}{d\Omega}(\mathbf{Q}) = \frac{N}{V}\cdot\left|\rho_{\text{single}}(\mathbf{Q})\right|^2 = (\Delta\rho)^2\,\phi_{\text{spheres}}\,V_{\text{sphere}}\,F(\mathbf{Q}) \tag{22}$$

$$F(\mathbf{Q}) = \left(3\frac{\sin(QR)-QR\cos(QR)}{(QR)^3}\right)^2 \tag{23}$$

We considered N independent spheres in our volume V, and thus obtained the concentration of spheres ϕ_{spheres}. Furthermore, we defined the form factor $F(Q)$, which describes the Q-dependent term for independent spheres (or the considered shapes in general). The function is shown in Figure 9. The first zero of the form factor is found at $Q = 4.493/R$. This relation again makes clear why the reciprocal space (Q-space) is called reciprocal. We know the limit for small scattering angles is $F(\mathbf{Q}\to 0) = 1 - \frac{1}{5}Q^2R^2$. So the form factor is normalized to 1, and the initial dependence on Q^2 indicates the size of the sphere. For large scattering angles the form factor is oscillating. Usually the instrument cannot resolve the quickest oscillations and an average intensity is observed. The asymptotic behavior would read $F(\mathbf{Q}\to\infty) = \frac{9}{2}(QR)^{-4}$. The obtained power law Q^{-4} is called Porod law and holds for any kind of bodies with sharp interfaces. So, sharp interfaces are interpreted as fractals with $d = 2$ dimensions, and the corresponding exponent is $6 - d$. The general appearance of the Porod formula reads then:

$$\frac{d\Sigma}{d\Omega}(Q) = P\cdot Q^{-4} \tag{24}$$

The amplitude of the Porod scattering P tells about the surface per volume and reads $P = 2\pi(\Delta\rho)^2 S_{\text{tot}}/V_{\text{tot}}$. Apart from the contrast, it measures the total surface S_{tot} per total volume V_{tot}. For our shperes, the Porod constant becomes $P = 2\pi(\Delta\rho)^2 4\pi R^2/(4\pi R^3/(3\phi)) =$

$6\pi\phi_1(\Delta\rho)^2/R$. The surface to volume ratio is smaller the larger the individual radius R is. The remaining scaling with the concentration ϕ_1 and the contrast $(\Delta\rho)^2$ arises still from the prefactor which we discussed in context with eq. 22.

When comparing the theoretical description of the spherical form factor with measurements one finds a good agreement (Fig. 10). Many fringes are seen, but after the third or fourth peak the function does not indicate any oscillation any more. Furthermore, the sharp minima are washed out. All of this is a consequence of the resolution function (eq. 5) which has been taken into account for the fitted curve. For many other examples one also needs to take the polydispersity into account. The synthesis of colloids usually produces a whole distribution of different radii. In our example the polydispersity is very low which is the desired case. Polydispersity acts in a similar way compared to the resolution function. The sharp minima are washed out. While the resolution appears as a distribution of different Q-values measured at a certain point the polydispersity integrates over several radii.

Another general scattering law for isolated (dilute) colloids is found for small scattering angles. The general appearance of the Guinier scattering law is:

$$\frac{d\Sigma}{d\Omega}(\mathbf{Q}\to 0) = \frac{d\Sigma}{d\Omega}(0) \cdot \exp\left(-\frac{1}{3}Q^2R_g^2\right) \tag{25}$$

When comparing the scattering law of a sphere and the Guinier formula we obtain $R_g = \sqrt{\frac{3}{5}}R$. The radius of gyration R_g can be interpreted as a momentum of inertia normalized to the total mass and specifies the typical size of the colloid of any shape. The Guinier formula can be seen as an expansion at small scattering angles of the logarithm of the macroscopic cross section truncated after the Q^2 term. Further details are discussed in Appendix A.

Another general appearance for independent colloids shall be discussed now using equation 22. The macroscopic cross section is determined by several important factors: The contrast between the colloid and the solvent given by $\Delta\rho^2$, the concentration of the colloids, the volume of a single colloid, and the form factor. Especially for small Q the latter factor turns to 1, and the first three factors dominate. When knowing two factors from chemical considerations, the third factor can be determined experimentally using small angle neutron scattering.

2.7 Scattering of a polymer

In this section we derive the scattering of a single (isolated) polymer coil. This model is the basis for many more complicated models of polymers in solution, polymeric micelles, polymer melts, diblock and multiblock copolymers and so on. So the understanding of these concepts is rather important for scattering experiments on any kind of polymer systems.

This example starts apart from many other calculations from point-like monomers (see eq. 10). These monomers are found along a random walk with an average step width of ℓ_K. We try to argue for non-ideal chain segments, but finally will arrive at an expression for rather ideal polymers. For the scattering function we obtain (definition of $S(Q)$ in eq. 37-39):

$$
\begin{aligned}
S(\mathbf{Q}) &\propto \frac{1}{N}\sum_{j,k=0}^{N}\Big\langle \exp\left(\mathrm{i}\mathbf{Q}\cdot(\mathbf{R}_j-\mathbf{R}_k)\right)\Big\rangle &(26)\\
&\propto \frac{1}{N}\sum_{j,k=0}^{N}\exp\left\langle -\tfrac{1}{2}\left(\mathbf{Q}\cdot(\mathbf{R}_j-\mathbf{R}_k)\right)^2\right\rangle &(27)\\
&\propto \frac{1}{N}\sum_{j,k=0}^{N}\exp\left\langle -\tfrac{1}{6}\mathbf{Q}^2\cdot(\mathbf{R}_j-\mathbf{R}_k)^2\right\rangle &(28)
\end{aligned}
$$

At this stage we use statistical arguments (i.e. statistical physics). The first rearrangement of terms (line 27) moves the ensemble average of the monomer positions (and distances $\Delta\mathbf{R}_{jk}$) from the outside of the exponential to the inside. This is an elementary step which is true for polymers. The underlying idea is, that the distance $\Delta\mathbf{R}_{jk}$ arises from a sum of $|j-k|$ bond vectors which all have the same statistics. So each sub-chain with the indices jk is only distinguished by its number of bond vectors inside. The single bond vector $\mathbf{b}_j$ has a statistical average of $\langle\mathbf{b}_j\rangle = 0$ because there is no preferred orientation. The next higher moment is the second moment $\langle\mathbf{b}_j^2\rangle = \ell_K^2$. This describes that each bond vector does a finite step with an average length of ℓ_K. For the sub-chain we then find an average size $\langle\Delta\mathbf{R}_{jk}^2\rangle = |j-k|\ell_K^2$. The reason is that in the quadrature of the sub-chain only the diagonal terms contribute because two distinct bond vectors show no (or weak) correlations.

Back to the ensemble average: The original exponential can be seen as a Taylor expansion with all powers of the argument $\mathrm{i}\mathbf{Q}\Delta\mathbf{R}_{jk}$. The odd powers do not contribute with similar arguments than for the single bond vector $\langle\mathbf{b}_j\rangle = 0$. Thus, the quadratic term is the leading term. The reason why the higher order terms can be arranged that they finally fit to the exponential expression given in line 27 is the weak correlations of two distinct bond vectors. The next line 28 basically expresses the orientational average of the sub-chain vector $\Delta\mathbf{R}_{jk}$ with respect to the Q-vector in three dimensions.

This derivation can be even simpler understood on the basis of a Gaussian chain. Then every bond vector follows a Gaussian distribution (with a center of zero bond length). Then the ensemble average has the concrete meaning $\langle\cdots\rangle = \int\cdots\exp\left(-\frac{3}{2}\Delta\mathbf{R}_{jk}^2/(|j-k|\ell_K^2)\right)d^3\Delta R_{jk}$. This distribution immediately explains the rearrangement of line 27. The principal argument is the central limit theorem: When embracing several segments as an effective segment any kind of distribution converges to yield a Gaussian distribution. This idea came from Kuhn who formed the term Kuhn segment. While elementary bonds still may have correlations at the stage of the Kuhn segment all correlations are lost, and the chain really behaves ideal. This is the reason why the Kuhn segment length ℓ_K was already used in the above equations.

In the following we now use the average length of sub-chains (be it Kuhn segments or not), and replace the sums by integrals which is a good approximation for long chains with a large number of segments N.

$$
\begin{aligned}
S(\mathbf{Q}) &\propto \frac{1}{N}\int_0^N dj\int_0^N dk\,\exp\left(-\tfrac{1}{6}\mathbf{Q}^2\cdot|j-k|\cdot\ell_K^2\right) &(29)\\
&= N\cdot f_D(Q^2R_g^2) &(30)
\end{aligned}
$$

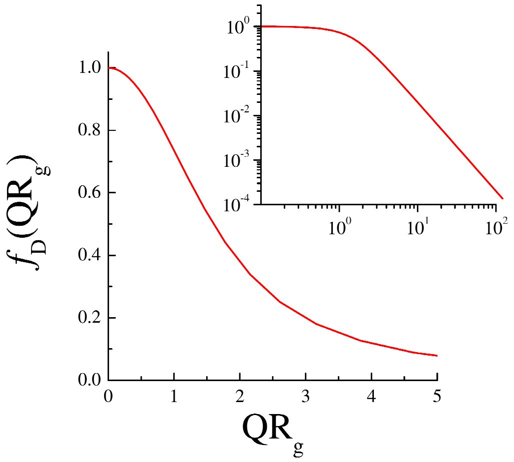

Fig. 11: *The theoretical Debye function describes the polymer scattering of independent polymers without interaction. The two plots show the function on a linear and double logarithmic scale.*

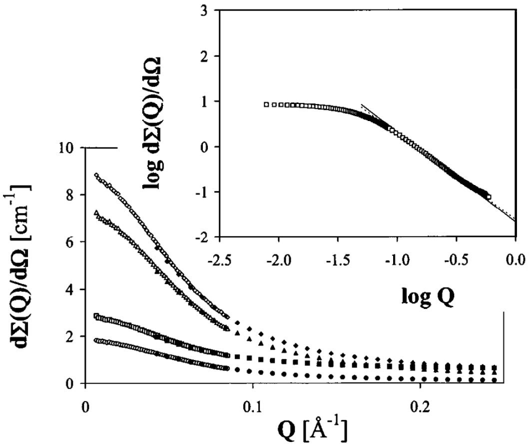

Fig. 12: *Scattering of a h/d-PDMS polymer blend. The linear scale shows different compositions of hydrogenous polymer (from bottom to top: 0.05, 0.94, 0.27, 0.65) while the double logarithmic plot shows the 0.65 sample only [5].*

$$f_D(x) = \frac{2}{x^2}\left(\exp(-x) - 1 + x\right) \qquad \text{with} \quad x = Q^2 R_g^2 \tag{31}$$

In this integral one has to consider the symmetry of the modulus. The result is basically the Debye function which describes the polymer scattering well from length scales of the overall coil down to length scales where the polymer becomes locally rigid (see Fig. 11). The covalent bonds of a carbon chain effectively contribute to a certain rigidity which will not be treated here. The radius of gyration describes the overall dimension of the chain and is $R_g = \sqrt{N/6}\,\ell_K$. The limits of the polymer scattering are found to be:

$$S(\mathbf{Q}) \propto N(1 - \tfrac{1}{3}Q^2R_g^2) \qquad \text{for small } Q \tag{32}$$

$$\propto N \cdot 2/(Q^2R_g^2) \qquad \text{for large } Q \tag{33}$$

The line 32 describes the conventional Guinier scattering of the overall polymer (compare eq. 25). The second line 33 describes a power law. At these length scales the sub-chains of different lengths are self-similar and so they reveal a fractal behavior. The prefactor is connected to the magnitude R_g^2/N which is the effective segment size. From this magnitude one can calculate back to the local rigidity which is responsible for the effective segments.

When we want to compare experiments with this theory the best examples are obtained from polymer blends (Fig. 12). One could come to the conclusion that diluted polymer solutions must provide the ideal conditions for such an experiment but practically the interactions of the solvent molecules with the monomers lead to a deviating behavior: The good solvent conditions lead to energetic violations of monomer-monomer contacts and so the polymer swells and displays a different fractal behavior. The high Q power law in good solvents comes close to $Q^{-1.7}$. The Flory theory was the first attempt to describe this behavior while many refinements find small corrections. The theoretically most precise Flory exponent is $\nu = 0.588$ which is the reciprocal value of the given exponent 1.7 above.

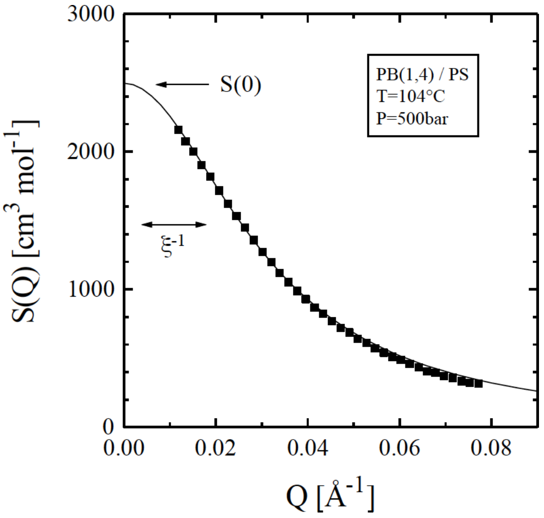

Fig. 13: *Typical scattering of a homopolymer blend with interactions. The sample is a polybutadiene(1,4) / polystyrene blend at 104°C and 500bar [6].*

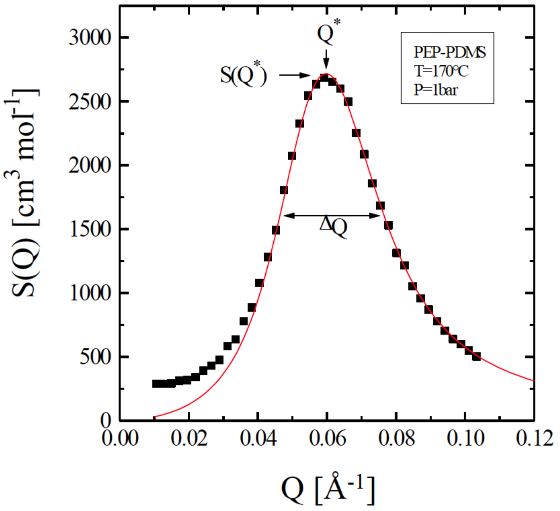

Fig. 14: *Typical scattering of a diblock copolymer blend with interactions [7]. The poly-ethylene-propylene–poly-dymethylsiloxane is heated to 170°C (1bar).*

So polymer blends are often better examples for weakly interacting chains. This finding is supported by the low entropy of mixing which enforces small interactions. The discussed example of Fig. 12 [5] considers the isotopic mixture of hydrogenous and deuterated polydimethylsiloxane (PDMS). This practically leads to one of the lowest possible interactions even though they are not completely zero. The theoretical concept of the random phase approximation is able to deal with interactions and describes phase diagrams and the scattering in this way. At high temperatures the polymers usually mix well, and the scattering comes closer to the weakly interacting case. Closer to the demixing temperature at lower temperatures the scattering intensity increases dramatically. This indicates strong composition fluctuations. The system loses the tendency to form a homogenous mixture and so local enrichments of species A or B are possible. While the random phase approximation is a mean field concept which describes weak fluctuations there are other concepts for strong fluctuations close to the phase boundary: The 3-dimensional Ising model – known for ferromagnets – describes the strong fluctuations of the two component polymer system.

The example of an interacting homopolymer blend is shown in Fig. 13. The general aspects are kept from non-interacting polymers (compare Fig. 12). The scattering curve has a maximum at $Q = 0$, and is decaying to large Q where a power law of Q^{-2} for ideal chains is observed. The maximal intensity is connected to the reciprocal susceptibility which describes the tendency of spontaneous thermal fluctuations to decay. High intensities mean low susceptibilies and strong fluctuations – the vice versa arguments are valid. The width of this curve is connected to the correlation length ξ. At low interactions it is tightly connected to the single coil size, i.e. R_g. With strong fluctuations close to the phase boundary the correlation length tends to diverge, which measures the typical sizes of the thermally fluctuating enrichments.

A diblock copolymer is a linear chain with two different monomer species. The first part is pure A and the latter pure B. The typical scattering of a diblock copolymer blend is shown in Fig. 14. At small Q the ideal scattering increases with Q^2 accordingly to the ‘correlation holeł. The chemistry of the molecule does not allow for enrichments of A or B on large length scales. A continuously growing volume would only allow for enrichments on the surface – this explains finally the exponent in the scattering law. The experimental finite intensities relate to imperfections of the molecules. The chain length ratio f is distributed, and finally allows for enrichments on large length scales.

The dominating fluctuations are found at a finite Q^*. This expresses that the coil allows for separations of A and B predominantly on the length scale of the overall coil. Close to the phase boundary and especially below (where the polymer undergoes a micro phase separation) the coils are stretched. The peak at finite Q^* also expresses that the fluctuations tend to form alternating enrichments. From a center it would look like a decaying order of A-B-A-B-... The width of the peak is again connected to the correlation length $\xi \sim \Delta Q^{-1}$ which describes the length of this decaying order. At high Q, again a Q^{-2} law is observed describing the sub-chains being ideal chains. On these length scales homopolymer blends and diblock copolymers do not differ.

The whole understanding of phase boundaries and fluctuations is important for applications. Many daily life plastic products consist of polymer blends since the final product should have combined properties of two different polymers. Therefore, polymer granulates are mixed at high temperatures under shear in an extruder. The final shape is given by a metal form where the polymer also cools down. This process involves a certain temperature history which covers the one-phase and two-phase regions. Therefore, the final product consists of many domains with almost pure polymers. The domain size and shape are very important for the final product. So the process has to be tailored in the right way to yield the specified domain structure. This tailoring is supported by a detailed knowledge of the phase boundaries and fluctuation behavior. Advanced polymer products also combine homopolymers and diblock copolymers for an even more precise and reproducible domain size/shape tailoring [8, 9]. The diblock copolymer is mainly placed at the domain interfaces, and, therefore, influences the domain properties precisely.

2.8 Contrast variation

For neutron scattering the method contrast variation opens a wide field of possible experiments. For soft matter research the most important labeling approach is the exchange of hydrogen ^{1}H by deuterium ^{2}H $\equiv$ D. Since in a single experiment the phase information is lost completely the contrast variation experiment retrieves this information partially. Relative positions of two components are obtained by this method.

The scattering length density of the overall sample is now understood to originate from each component individually. So the specific $\rho_j(\mathbf{r})$ takes the value of the scattering length density of component j when the location points to component j and is zero otherwise. We would then obtain the following:

$$\rho(\mathbf{Q}) = \int\limits_V d^3r \, \left(\sum_{j=1}^{n} \rho_j(\mathbf{r}) \right) \exp(\mathrm{i}\mathbf{Q}\mathbf{r}) \tag{34}$$

n specifies the number of components. The assumption of incompressibility means that on every place there is one component present, and so all individual functions $\rho_j(\mathbf{r})$ fill the full space. Furthermore, we would like to define component 1 being the reference component, i.e. $\rho_{\mathrm{ref}} = \rho_1$ (see eq. 16). This means that on each place we have a $\Delta\rho_j(\mathbf{r})$ function similar to eq. 17. Then, we arrive at:

$$\rho(\mathbf{Q}) = \sum_{j=2}^{n} \Delta\rho_{j1}(\mathbf{Q}) \tag{35}$$

The macroscopic cross section is a quadrature of the scattering length density $\rho(\mathbf{Q})$, and so we arrive at:

$$\begin{aligned} \frac{d\Sigma}{d\Omega}(\mathbf{Q}) &= \frac{1}{V} \cdot \sum_{j,k=2}^{n} \Delta\rho^*_{j1}(\mathbf{Q}) \cdot \Delta\rho_{k1}(\mathbf{Q}) && (36) \\ &= \sum_{j,k=2}^{n} (\Delta\rho_{j1}\Delta\rho_{k1}) \cdot S_{jk}(\mathbf{Q}) && (37) \\ &= \sum_{j=2}^{n} (\Delta\rho_{j1})^2 \cdot S_{jj}(\mathbf{Q}) \;+\; 2 \sum_{2<j<k\leq n} (\Delta\rho_{j1}\Delta\rho_{k1}) \cdot \Re\, S_{jk}(\mathbf{Q}) && (38) \end{aligned}$$

In line 37 the scattering function $S_{jk}(\mathbf{Q})$ is defined. By this the contrasts are separated from the Q-dependent scattering functions. Finally, in line 38 the diagonal and off-diagonal terms are collected. There are $n-1$ diagonal terms, and $\frac{1}{2}(n-1)(n-2)$ off-diagonal terms. Formally, these $\frac{1}{2}n(n-1)$ considerably different terms are rearranged (the combinations $\{j,k\}$ are now simply numbered by j), and a number of s different measurements with different contrasts are considered.

$$\left.\frac{d\Sigma}{d\Omega}(\mathbf{Q})\right|_s = \sum_j (\Delta\rho\cdot\Delta\rho)_{sj} \cdot S_j(\mathbf{Q}) \tag{39}$$

In order to reduce the noise of the result, the number of measurements s exceeds the number of independent scattering functions considerably. The system then becomes over-determined when solving for the scattering functions. Formally, one can nonetheless write:

$$S_j(\mathbf{Q}) = \sum_s (\Delta\rho\cdot\Delta\rho)^{-1}_{sj} \cdot \left.\frac{d\Sigma}{d\Omega}(\mathbf{Q})\right|_s \tag{40}$$

The formal inverse matrix $(\Delta\rho\cdot\Delta\rho)^{-1}_{sj}$ is obtained by the singular value decomposition method. It describes the closest solution of the experiments in context of the finally determined scattering functions.

An example case is discussed for a bicontinuous microemulsion with an amphiphilic polymer [10]. The microemulsion consists of oil and water domains which have a sponge structure. So the water domains host the oil and vice versa. The surfactant film covers the surface between the oil and water domains. The symmetric amphiphilic polymer position and function was not clear beforehand. From phase diagram measurements it was observed that the polymer increases the efficiency of the surfactant dramatically. Much less surfactant is needed to solubilize equal amounts of oil and water. Fig. 15 discusses the meaning of the cross terms of the scattering functions. Especially the film-polymer scattering is highly interesting to reveal the polymer role inside the microemulsion (see Fig. 16). By the modeling it was clearly observed that the amphiphilic polymer is anchored in the membrane and the two blocks describe a mushroom inside the oil and water domains. So basically, the polymer is a macro-surfactant. The coils of the polymer exert a certain pressure on the membrane and keep it flat. The membrane with less

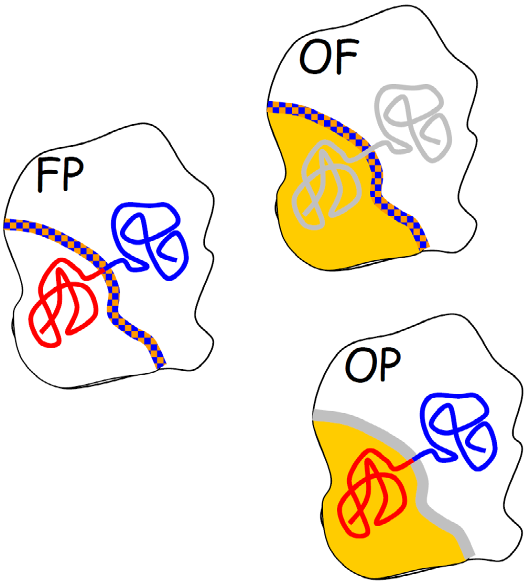

Fig. 15: *Scheme of scattering functions for the cross terms within the microemulsion. There are the film-polymer scattering S_{FP}, the oil-film scattering S_{OF}, and the oil-polymer scattering S_{OP}. The real space correlation function means a convolution of two structures.*

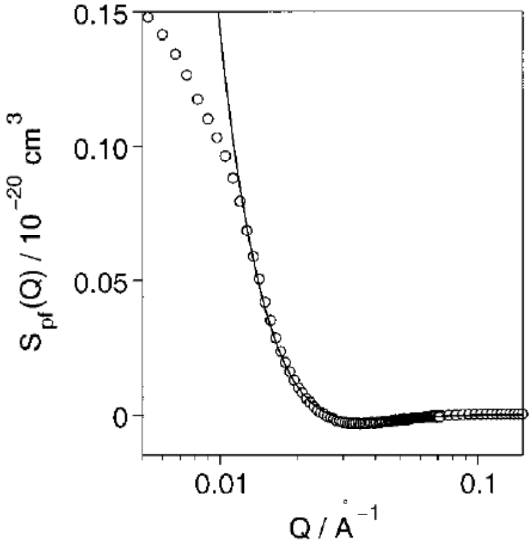

Fig. 16: *A measurement of the film-polymer scattering for a bicontinuous microemulsion with a symmetric amphiphilic polymer. The solid line is described by a polymer anchored in the film. The two blocks are mushroom-like in the domains. At low Q the overall domain structure (or size) limits the idealized model picture.*

fluctuations allows for the formation of larger domains with a better surface to volume ratio. This is finally the explanation how the polymer acts as an efficiency booster.

3 Small Angle X-ray Scattering

While a detailed comparison between SANS and SAXS is given below, the most important properties of the small angle x-ray scattering technique shall be discussed here. The x-ray sources can be x-ray tubes (invented by Röntgen, keyword Bremsstrahlung) and modern synchrotrons. The latter ones guide fast electrons on undulators which act as laser-like sources for x-rays with fixed wavelength, high brilliance and low divergence. This simply means, that the collimation of the beam often yields narrow beams, and the irradiated sample areas are considerably smaller (often smaller than ca. $1 \times 1\mathrm{mm}^2$). A view on the sample position is given in Fig. 17 (compare Fig. 3). One directly has the impression that all windows are tiny and adjustments must be made more carefully.

The conceptual understanding of the scattering theory still holds for SAXS. For the simplest understanding of the contrast conditions in a SAXS experiment, it is sufficient to count the electron numbers for each atom. The resulting scattering length density reads then (compare eq. 12):

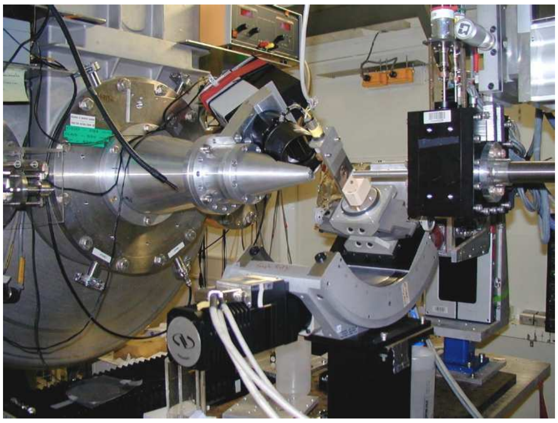

Fig. 17: *The sample position of the SAXS instrument ID2 at the ESRF, Grenoble, France. The photons propagate from the right to the left. The collimation guides on the left and the detector tank window on top of the cone on the left give an impression about the small beam size (being typically 1×1mm^2).*

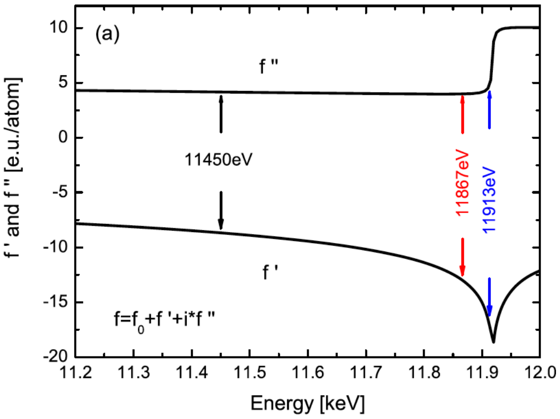

Fig. 18: *The complex dispersion curve for gold (Au) at the L$_3$ edge [11]. The overall effective electron number $f = f_0 + f' + \mathrm{i}f''$ replaces the conventional electron number $Z = f_0$ in equation 41. On the x-axis the energies of the x-rays is shown, with indications for the experimentally selected three energies (black, red, blue). In this way, equal steps for the contrast variation are achieved.*

$$\rho_{\mathrm{mol}} = \frac{r_e}{V_{\mathrm{mol}}} \sum_{j \in \{\mathrm{mol}\}} Z_j \tag{41}$$

The classical electron radius is $r_e = \mathrm{e}^2/(4\pi\epsilon_0 m_e c^2) = 2.82\mathrm{fm}$. The electron number of each atom j is Z_j. This means that chemically different substances have a contrast, but for similar substances (often for organic materials) it can be rather weak. Heavier atoms against light materials are much easier to detect. Finally, the density of similar materials is also important. Especially for organic materials (soft matter research), the high intensity of the source still allows for collecting scattering data. Many experiments base on these simple modifications with respect to SANS, and so the fundamental understanding of SAXS experiments does not need any further explanation.

For completeness, we briefly discuss the scattering length density for light scattering. Here the polarizability plays an important role. Without going into details, the final contrast is expressed by the refractive index increment dn/dc:

$$\rho_{\mathrm{mol}} = \frac{2\pi n}{\lambda^2} \cdot \frac{dn}{dc_{\mathrm{mol}}} \tag{42}$$

The refractive index increment dn/dc finally has to be determined separately experimentally when the absolute intensity is of interest. The concentration c_{mol} is given in units volume per volume (for the specific substance in the solvent). The wavelength of the used light is λ.

3.1 Contrast variation using anomalous small angle x-ray scattering

While for contrast variation SANS experiments the simple exchange of hydrogen ^{1}H by deuterium ^{2}H $\equiv$ D allowed for changing the contrast without modifying the chemical behavior, in contrast variation SAXS experiments the applied trick is considerably different: The chemistry is mainly dominated by the electron or proton number Z and isotope exchange would not make any difference. The electron shells on the other hand have resonances with considerable dispersion curves. An example is shown in Fig. 18 with the real part f' (called dispersion) and the imaginary part f'' (called absorption). The overall effective electron number $f = f_0 + f' + \mathrm{i}f''$ replaces the conventional electron number $Z = f_0$ in equation 41. Below the resonance energy the considered L_3 shell appears only softer and effectively less electrons appear for f. Above the resonance energy single electrons can be scattered out from the host atom (Compton effect). This is directly seen in the sudden change of the absorption. Furthermore, the actual dependence of the dispersion is influenced by backscattering of the free electrons to the host atom (not shown in Fig. 41). This effect finally is the reason that the complex dispersion curve can only theoretically be well approximated below the resonance (or really far above). For this approximation it is sufficient to consider isolated host atoms.

For best experimental results the f-values have to be equally distributed. Thus, the energies are selected narrower close to the resonance (see Fig. 41). The investigated sample consisted of core-shell gold-silver nanoparticles in soda-lime silicate glass (details in reference [11]). By the contrast variation measurement one wanted to see the whole particles in the glass matrix, but also the core-shell structure of the individual particles. Especially, the latter one would be obtained from such an experiment. First results of this experiment are shown in Fig. 19. The most important result from this experiment is that the original scattering curves at first hand do not differ considerably. The core-shell structure results from tiny differences of the measurements. For contrast variation SANS experiments the contrasts can be selected close to zero contrast for most of the components which means that tiniest amounts of additives can be highlighted and the intensities between different contrasts may vary by factors of 100 to 1000. So for contrast variation SAXS measurements the statistics have to be considerably better which in turn comes with the higher intensities.

Another example was evaluated to a deeper stage [12]. Here, the polyelectrolyte polyacrylate (PA) with Sr^{2+} counterions was dissolved in water. The idea behind was that the polymer is dissolved well in the solvent. The charges of the polymer and the ions lead to a certain swelling of the coil (exact fractal dimensions ν not discussed here). The counterions form a certain cloud around the chain – the structure of which is the final aim of the investigation. The principles of contrast variation measurements leads to the following equation (compare eq. 39):

$$\frac{d\Sigma}{d\Omega} = (\Delta\rho_{\mathrm{Sr-H2O}})^2 \cdot S_{\mathrm{Sr-Sr}} \; + \; (\Delta\rho_{\mathrm{PA-H2O}})^2 \cdot S_{\mathrm{PA-PA}} \; + \; \Delta\rho_{\mathrm{Sr-H2O}}\Delta\rho_{\mathrm{PA-H2O}} \cdot S_{\mathrm{Sr-PA}} \quad (43)$$

The overall scattering is compared with two contributions in Fig. 20. The scattering functions of the cross term $S_{\mathrm{Sr-PA}}$ and the pure ion scattering $S_{\mathrm{Sr-Sr}}$ have been compared on the same scale, and so the contrasts are included in Fig. 20. Basically, all three functions describe a polymer coil in solvent – the different contrasts do not show fundamental differences. Nonetheless, a particular feature of the ion scattering was highlighted by this experiment: At $Q \approx 0.11\mathrm{nm}^{-1}$ is a small maximum which is connected to the interpretation of effective charge beads along the chains. The charge clouds obviously can be divided into separated beads. The emphasis of the observed maximum correlates with the number of beads: For small numbers it is invisible,

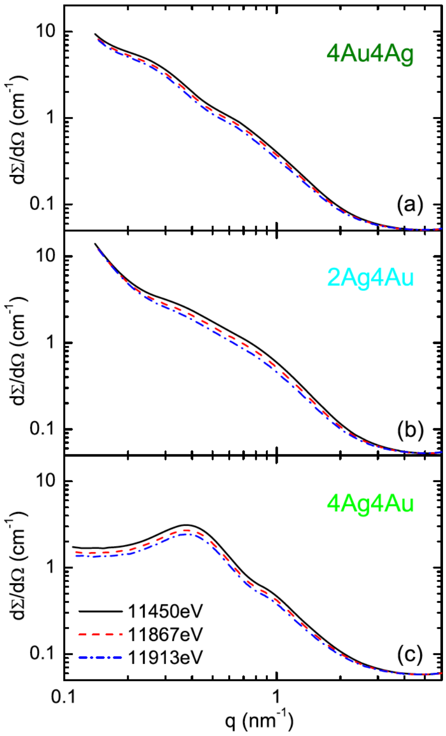

Fig. 19: *Absolute calibrated scattering curves of different core-shell Ag/Au nanoparticles in soda-lime silicate glass [11]. The implantation sequence has been changed for the three samples. Note that the three scattering curves for the selected energies (colors correspond to Fig. 18) do only slightly differ due to the small changes of the contrast.*

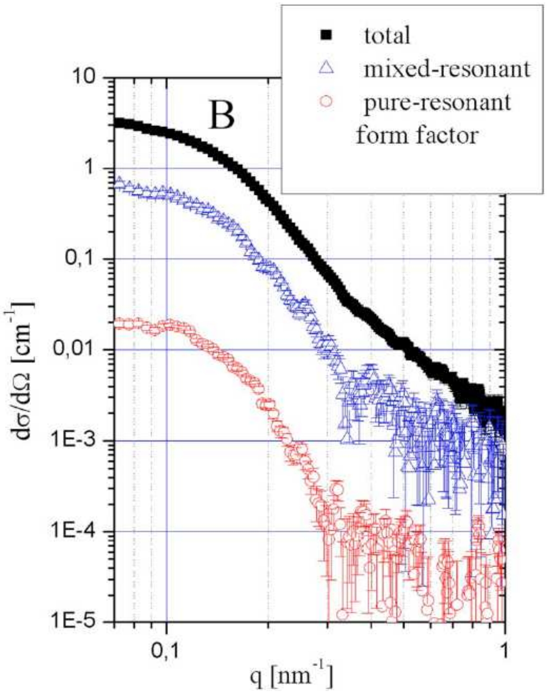

Fig. 20: *Further evaluated scattering functions of a different system [12]: A polyelectrolyte with Sr^{2+} counterions in aqueous solution. The top curve (black) indicates the overall scattering. The middle curve (blue) displays the polymer-ion cross terms being sensitive for relative positions. The bottom curve (red) depicts the pure ion scattering.*

and becomes more pronounced with higher numbers. The authors finally find that the number of 5 beads is suitable for the description of the scattering curves: An upper limit is also given by the high Q scattering where the 5 chain segments appear as independent sub-coils. This example beautifully displays, that the method of contrast variation can be transferred to SAXS experiments. Difficulties of small contrast changes have been overcome by the good statistics due to much higher intensities.

4 Comparison of SANS and SAXS

We have seen that many parallels exist between the two experimental methods SANS and SAXS. The theoretical concepts are the same. Even the contrast variation method as a highly difficult and tedious task could be applied for both probes. In the following, we will highlight differences that have been discussed so far and others that are just mentioned now.

The high flux reactors are at the technical limit of highest neutron fluxes. For SANS instruments maximal fluxes of ca. 2×10^8 neutrons/s/cm^2 have been reached at the sample position. Typical sample sizes are of 1×1cm^2. For coherent scattering fractions of ca. 10% this results in maximal count rates of 10^7Hz, while practically most of the count rates stay below 10^6Hz. For long collimations, the experimentalists deal often with 10 to 50Hz. The resolution for these count rates has been relaxed. Wavelength spreads of either ±5% or ±10% are widely accepted, and the collimation contributes equally, such that a typical resolution of $\Delta Q/Q$ of 7 to 14% is reached. For many soft matter applications this is more than adequate. If one thinks of liquid crystalline order, much higher resolution would be desired which one would like to overcome by choppers in combination with time-of-flight analysis. A resolution of ca. 1% would be a reasonable expectation. The continuous sources are highly stable which is desired for a reliable absolute calibration.

The spallation sources deliver either continuous beams or the most advanced ones aim at pulsed beams. Repetition rates range from ca. 14 to 60Hz. The intensity that is usable for SANS instruments could reach up to 20 times higher yields (as planned for the ESS in Lund), i.e. up to 4×10^9 neutrons/s/cm^2. Surely, detectors for count rates of 10 to 100 MHz have to be developed. The new SANS instruments will make use of the time-of-flight technique for resolving the different wavelengths to a high degree. Of course other problems with such a broad wavelength band have to be overcome – but this topic would lead too far.

The synchrotron sources reach much higher photon yields which often makes the experiments technically comfortable but for the scientist at work highly stressful. The undulators provide laser-like qualities of the radiation which explains many favorable properties. Some numbers for the SAXS beam line ID2 at the ESRF shall be reported. The usable flux of 5×10^{15} photons/s/mm^2 (note the smaller area) is provided which results for a typical sample area of ca. 1×0.02mm^2 in 10^{14} photons/s. In some respect the smallness of the beam urges to think about the representativeness of a single shot experiment. At some synchrotron sources the beam is not highly stable which makes absolute calibration and background subtraction difficult. The same problem also occurs for the pulsed neutron sources where parts of the calibration procedure become highly difficult.

For classical SANS experiments one can make some statements: The absolute calibration is practically done for all experiments and does not take much effort – it is technically simple. Between different instruments in the world the discrepancies of different calibrations results often in errors of 10% and less. Part of the differences are different calibration standards, but also different concepts for transmission measurements and many details of the technical realization. The nuclear scattering is a result of the fm small nuclei and results in easily interpretable scattering data for even large angles – for point-like scatterers no corrections have to be made. In this way all soft matter and biological researchers avoid difficult corrections. Magnetic structures can be explored by neutrons due to its magnetic moment. Magnetic scattering is about to be implemented to a few SANS instruments. Ideally, four channels are experimentally measured (I_{++}, I_{+-},I_{-+}, and I_{--}) by varying the polarization of the incident beam (up/down) and of the analyzer. Nowadays, the ^{3}He technique allows for covering relatively large exit angles at high polarization efficiencies. But also early magnetic studies have been possible with simpler setups and reduced information. The unsystematic dependence of the scattering length often opens good conditions for a reasonable contrast for many experiments. If the natural isotopes do not provide enough contrast pure isotopes might overcome the problem. The contrast variation experiments have been presented for the SANS technique. By a simple exchange of hydrogen by deuterium, soft matter samples can be prepared for complicated contrast variation experiments. One advantage is the accessibility of the zero contrast for most of the components which allows for highlighting smallest amounts of additives. The high demand for deuterated chemicals makes them cheap caused by the huge number of NMR scientists. The low absorption of neutrons for many materials allows for studying reasonably thick samples (1 to 5mm and beyond). Especially, for contrast variation experiments often larger optical path lengths are preferred. The choice for window materials and sample containers is simple in many cases. Neutron scattering is a non-destructive method. Espeically biological samples can be recovered.

Contrarily we observe for the SAXS technique: The demand for absolute calibration in SAXS experiments is growing. Initial technical problems are overcome and suitable calibration standards have been found. The interpretation of scattering data at larger angles might be more complicated due to the structure of the electron shells. For small angle scattering the possible corrections are often negligible. Magnetic structures are observable by the circular magnetic dichroism [13] but do not count to the standard problems addressed by SAXS. The high contrast of heavy atoms often makes light atoms invisible. For soft matter samples the balanced use of light atoms results in low contrast but, technically, the brilliant sources overcome any intensity problem. The ASAXS technique is done close to resonances of single electron shells and opens the opportunity for contrast variation measurements. The achieved small differences in the contrast still allow for tedious measurements because the statistics are often extremely good – only stable experimental conditions have to be provided. The absorption of x-rays makes the choice of sample containers and windows more complicated. The absorbed radiation destroys the sample in principle. Short experimental times are thus favorable.

To summarize, the method of small angle neutron scattering is good-natured and allows to tackle many difficult tasks. The small angle x-ray scattering technique is more often applied due to the availability. Many problems have been solved (or will be solved) and will turn to standard techniques. So, in many cases the competition between the methods is kept high for the future. Today, practically, the methods are complementary and support each other for the complete structural analysis.

Appendices

A Guinier Scattering

The crucial calculation of the Guinier scattering is done by a Taylor expansion of the logarithm of the macroscopic cross section for small scattering vectors Q. Due to symmetry considerations there are no linear terms, and the dominating term of the Q-dependence is calculated to be:

$$
\begin{aligned}
R_g^2 &= -\frac{1}{2}\cdot\frac{\partial^2}{\partial Q^2}\ln\Big(\rho(\mathbf{Q})\rho(-\mathbf{Q})\Big)\bigg|_{\mathbf{Q}=0} && (44)\\
&= -\frac{1}{2}\cdot\frac{\partial}{\partial Q}\frac{2\Re\big(\rho(\mathbf{Q})\int d^3r\ \rho(\mathbf{r})(-\mathrm{i}\mathbf{r})\exp(-\mathrm{i}\mathbf{Q}\mathbf{r})\big)}{\rho(\mathbf{Q})\rho(-\mathbf{Q})}\Bigg|_{\mathbf{Q}=0} && (45)\\
&= -\Re\frac{\rho(\mathbf{Q})\int d^3r\ \rho(\mathbf{r})(-\mathbf{r}^2)\exp(-\mathrm{i}\mathbf{Q}\mathbf{r})}{\rho(\mathbf{Q})\rho(-\mathbf{Q})}\bigg|_{\mathbf{Q}=0}\\
&\quad -\Re\frac{\int d^3r\ \rho(\mathbf{r})(\mathrm{i}\mathbf{r})\exp(\mathrm{i}\mathbf{Q}\mathbf{r})\int d^3r\ \rho(\mathbf{r})(-\mathrm{i}\mathbf{r})\exp(-\mathrm{i}\mathbf{Q}\mathbf{r})}{\rho(\mathbf{Q})\rho(-\mathbf{Q})}\bigg|_{\mathbf{Q}=0}\ +\ 0 && (46)\\
&= \langle\mathbf{r}^2\rangle-\langle\mathbf{r}\rangle^2 && (47)\\
&= \Big\langle\big(\mathbf{r}-\langle\mathbf{r}\rangle\big)^2\Big\rangle && (48)
\end{aligned}
$$

The first line 44 contains the definition of the Taylor coefficient. Then, the derivatives are calculated consequently. Finally, we arrive at terms containing the first and second momenta. The last line 48 rearranges the momenta in the sense of a variance. So the radius of gyration is the second moment of the scattering length density distribution with the center of 'gravity' being at the origin. We used the momenta in the following sense:

$$
\begin{aligned}
\langle\mathbf{r}\rangle &= \int d^3r\ \mathbf{r}\rho(\mathbf{r})\bigg/\int d^3r\ \rho(\mathbf{r}) && (49)\\
\langle\mathbf{r}^2\rangle &= \int d^3r\ \mathbf{r}^2\rho(\mathbf{r})\bigg/\int d^3r\ \rho(\mathbf{r}) && (50)
\end{aligned}
$$

So far we assumed an isotropic scattering length density distribution. In general, for oriented anisotropic particles, the Guinier scattering law would read:

$$
\frac{d\Sigma}{d\Omega}(\mathbf{Q}\!\to\!0)=\frac{d\Sigma}{d\Omega}(0)\cdot\exp\Big(-Q_x^2\Big\langle\big(x-\langle x\rangle\big)^2\Big\rangle-Q_y^2\Big\langle\big(y-\langle y\rangle\big)^2\Big\rangle-Q_z^2\Big\langle\big(z-\langle z\rangle\big)^2\Big\rangle\Big) \tag{51}
$$

Here, we assumed a diagonal tensor of second moment. This expression allows for different widths of scattering patterns for the different directions. In reciprocal space large dimensions appear small and vice versa. Furthermore, we see that R_g is defined as the sum over all second momenta, and so in the isotropic case a factor $\frac{1}{3}$ appears in the original formula 25.

References

[1] R.-J. Roe, *Methods of X-ray and Neutron Scattering in Polymer Science* (Oxford University Press, New York, 2000).

[2] J.S. Higgins, H.C. Benoît, *Polymers and Neutron Scattering* (Clarendon Press, Oxford, 1994).

[3] J. Skov Pedersen, D. Posselt, K. Mortensen, *J. Appl. Cryst.* **23**, 321 (1990).

[4] T. Vad, W.F.C. Sager, J. Zhang, J. Buitenhuis, A. Radulescu, *J. Appl. Cryst.* **43**, 686 (2010).

[5] S. Gagliardi, V. Arrighi, R. Ferguson, A.C. Dagger, J.A. Semlyen, J.S. Higgins, *J. Chem. Phys.* **122**, 064904 (2005).

[6] H. Frielinghaus, D. Schwahn, L. Willner, *Macromolecules* **34**, 1751 (2001).

[7] H. Frielinghaus, D. Schwahn, K. Mortensen, K. Almdal, T. Springer, *Macromolecules* **29**, 3263 (1996).

[8] J.H. Lee, M.L. Ruegg, N.P.Balsara, Y. Zhu, S.P. Gido, R. Krishnamoorti, M.H. Kim *Macromolecules* **36**, 6537 (2003) and B.J. Reynolds, M.L. Ruegg, N.P. Balsara, C.J. Radke, T.D. Shaffer, M.Y. Lin, K.R. Shull, D.J. Lohse *Macromolecules* **37**, 7410 (2004)

[9] N.R. Washburn, T.P. Lodge, F.S. Bates *J. Phys. Chem. B* **104**, 6987 (2000)

[10] H. Endo, M. Mihailescu, M. Monkenbusch, J. Allgaier, G. Gompper, D. Richter, B. Jakobs, T. Sottmann, R. Strey, I. Grillo, *J. Chem. Phys.* **115**, 580 (2001).

[11] J. Haug, H. Kruth, M. Dubiel, H. Hofmeister, S. Haas, D. Tatchev, A. Hoell, *Nanotechnology* **20**, 505705 (2009).

[12] G. Goerigk, K. Huber, R. Schweins, *J. Chem. Phys.* **127**, 154908 (2007) and G. Goerigk, R. Schweins, K. Huber, M. Ballauff, *Europhys. Lett.* **66**, 331 (2004).

[13] P. Fischer, R. Zeller, G. Schütz, G. Goerigk, H.G. Haubold, *J. Phys. IV France* **7**, C2-753 (1997).